NANO · MICRO small
www.small-journal.com

Revealing Site Occupancy in a Complex Oxide: Terbium Iron Garnet

Ethan Rosenberg, Jackson Bauer, Eunsoo Cho, Abinash Kumar, Jonathan Pelliciari, Connor A Occhialini, Shuai Ning, Allison Kaczmarek, Richard Rosenberg, John W. Freeland, Yu-Chia Chen, Jian-Ping Wang, James LeBeau, Riccardo Comin, F. M. F. de Groot, and Caroline A Ross**

Complex oxide films stabilized by epitaxial growth can exhibit large populations of point defects which have important effects on their properties. The site occupancy of pulsed laser-deposited epitaxial terbium iron garnet (TbIG) films with excess terbium (Tb) is analyzed, in which the terbium:iron (Tb:Fe) ratio is 0.86 compared to the stoichiometric value of 0.6. The magnetic properties of the TbIG are sensitive to site occupancy, exhibiting a higher compensation temperature (by 90 K) and a lower Curie temperature (by 40 K) than the bulk $Tb_3Fe_5O_{12}$ garnet. Data derived from X-ray core-level spectroscopy, magnetometry, and molecular field coefficient modeling are consistent with occupancy of the dodecahedral sites by Tb^{3+}, the octahedral sites by Fe^{3+}, Tb^{3+} and vacancies, and the tetrahedral sites by Fe^{3+} and vacancies. Energy dispersive X-ray spectroscopy in a scanning transmission electron microscope provides direct evidence of Tb_{Fe} antisites. A small fraction of Fe^{2+} is present, and oxygen vacancies are inferred to be present to maintain charge neutrality. Variation of the site occupancies provides a path to considerable manipulation of the magnetic properties of epitaxial iron garnet films and other complex oxides, which readily accommodate stoichiometries not found in their bulk counterparts.

1. Introduction

Complex oxides, which comprise cations of more than one element or valence state, represent a large class of materials with useful electronic properties such as superconductivity,[1] magnetism,[2] ferroelectricity,[3] magnetoresistance,[4,5] metal-insulator transitions,[6] catalytic activity,[7,8] and ionic transport.[9,10] Point defects in complex oxides perturb the structure, local coordination, and electronic configuration, strongly influencing the properties of the material. Multiple types of defects may be present, including substitutional or interstitial species, antisite defects, ions with valence changes, and cation or anion vacancies, with interdependent concentrations due to charge balance or defect reactions. Epitaxial growth of oxide films can stabilize crystal structures with large deviations from the bulk stoichiometry leading to elevated defect populations. An example

---

E. Rosenberg, J. Bauer, E. Cho, A. Kumar, A. Kaczmarek, J. LeBeau, C. A. Ross
Department of Materials Science and Engineering
Massachusetts Institute of Technology
Cambridge, MA 02139, USA
E-mail: errosen@mit.edu; caross@mit.edu

E. Rosenberg
3M Corporate Research Materials Laboratory
3M Center, St. Paul, MN 55114, USA

J. Pelliciari, C. A. Occhialini, R. Comin
Department of Physics
Massachusetts Institute of Technology
Cambridge, MA 02139, United States

J. Pelliciari
National Synchrotron Light Source II
Brookhaven National Laboratory
Upton, NY 11973, USA

S. Ning
School of Materials Science and Engineering
Nankai University
Tianjin 300350, P. R. China

R. Rosenberg, J. W. Freeland
Advanced Photon Source
X-Ray Science Division
Argonne National Laboratory
Lemont, IL 60439, USA

Y.-C. Chen, J.-P. Wang
Department of Electrical and Computer Engineering
University of Minnesota
Minneapolis, Minnesota 55455, USA

F. M. F. de Groot
Materials Chemistry and Catalysis
Utrecht University
Universiteitslaan 99, Utrecht 3584 CG, Netherlands

The ORCID identification number(s) for the author(s) of this article can be found under https://doi.org/10.1002/smll.202300824.

DOI: 10.1002/smll.202300824

© 2023 Wiley-VCH GmbH

is perovskite-structured yttrium orthoferrite, which has Y:Fe close to 1 in bulk (i.e., $YFeO_3$) but which can be grown epitaxially on $SrTiO_3$ with Y:Fe of 0.6–1.2, accommodated by high concentrations of antisite defects and vacancies.[11]

The variety of point defects and their influence on material properties present both challenges and opportunities for materials designers.[12,13] Considerable work has focused on point-defect engineering in perovskite-based structures, spinels, and other common crystal types.[14–17] Iron garnets ($R_3Fe_5O_{12}$) represent another important class of complex oxides. Iron garnets feature three cation sites: dodecahedral sites that accommodate the larger R^{3+} cations such as rare earth (RE) ions, Y, and Bi; and octahedral and tetrahedral sites filled with Fe^{3+}, allowing for a wide range of possible point defects on each site. Thin films of iron garnets have been studied intensively for spintronic and magneto-optical applications, and have shown perpendicular magnetic anisotropy,[18–23] fast spin-orbit torque-driven domain wall motion,[24,25] chiral magnetic textures,[26,27] and a high magneto-optical figure of merit,[28] among other useful properties. The equilibrium pseudobinary phase diagrams of Fe_2O_3-Y_2O_3, Fe_2O_3-Sm_2O_3, etc., imply that bulk iron garnets tolerate only small deviations of the R:Fe ratio away from 3:5, and form secondary phases when nonstoichiometric (hematite or yttrium orthoferrite in the case of yttrium iron garnet, YIG).[29,30] However, epitaxial thin film iron garnets have been reported with considerable deviation from bulk stoichiometry.[19–21,31,32] Understanding the defect types and concentrations present in iron garnet films is not only the key to designing their magnetic properties for spintronic and magnetooptical applications but also yields insight into how complex oxide thin films accommodate nonstoichiometry that would be unstable in the bulk.

In this work, we show that the concentrations of vacancies and antisite defects in a RE iron garnet (REIG) film can be determined from magnetic and structural data and that the compensation temperature in particular is a highly sensitive probe of the populations of point defects. Several REIGs, including RE = Gd, Tb, and Dy, exhibit a magnetic compensation temperature (T_{comp}) at which the magnetic moments of the sublattices sum to zero and the net magnetization is zero, as well as an angular momentum compensation point T_A where the net angular momentum is zero. Magnetic materials exhibit interesting behavior near these compensation temperatures, for example, fast dynamics[33] and efficient spin-orbit torque switching[34] in compensated metallic ferrimagnets, and fast domain wall velocities,[35] enhanced magnon–magnon coupling,[36] and noncollinear magnetism[37] in compensated insulator ferrimagnets. Control of T_{comp} and T_A is essential for designing materials for applications that take advantage of these properties. Several authors have reported that the T_{comp} of thin films of REIGs differs from that of the bulk garnet. Epitaxial terbium iron garnet (TbIG) thin films grown on gadolinium gallium garnet (GGG) by pulsed laser deposition (PLD) exhibited $T_{\mathrm{comp}} \approx 330$ K,[19] which is ≈80 K higher than the bulk T_{comp} of 250 K,[38] and TmIG was reported with $T_{\mathrm{comp}} = 75$ K[39] even though bulk TmIG does not have a compensation temperature.[18,38] PLD-grown single-crystal DyIG/GGG had $T_{\mathrm{comp}} = 190$ K[22] whereas bulk DyIG has $T_{\mathrm{comp}} = 220$ K.[38] PLD-grown polycrystalline GdIG showed $T_{\mathrm{comp}} = 377$ K, ≈100 K higher than that of bulk GdIG.[40] Sputtered Tb-deficient TbIG films showed T_{comp} 25–60 K below that of bulk TbIG.[41] In other studies, the T_{comp} of thin films matched that of bulk such as polycrystalline DyIG[22] and single crystal and polycrystalline TbIG.[28,42] Despite the substantial and growing popularity of garnets with compensation temperatures as objects of study, these surprising results have largely gone unexplained in the literature. Some studies (such as[19] and[41]) have suggested that a deviation of the RE:Fe ratio may provide an explanation for a non-bulk compensation temperature. However, these studies have stopped short of a quantitative model of this proposed effect.

In each formula unit of a stoichiometric REIG (**Figure 1**c), three RE^{3+} ions occupy dodecahedral sites while Fe^{3+} ions occupy two octahedral (Fe_{oct}) and three tetrahedral (Fe_{tet}) sites. The octahedral Fe and the RE sublattices couple antiparallel to the tetrahedral Fe sublattice making the material ferrimagnetic, and the net magnetic moment is given by $|(3\mu(\mathrm{RE}) + 2\mu(\mathrm{Fe_{oct}})) - 3\mu(\mathrm{Fe_{tet}})|$[38] where $\mu(X)$ represents the temperature-dependent magnetic moment of ion X. Changes in sublattice occupancy affect the net magnetization and compensation temperature; for example, Ga substitution into YIG can yield a compensated (antiferromagnetic) YGaIG,[43] while depletion of Gd in sputtered GdIG due to the precipitation of a Gd_2O_3 secondary phase increased T_{comp}.[44] Substitution of Ce, Bi, and Sc ions into PLD-grown TbIG influences both T_{comp} and the Curie temperature T_{Curie} of TbIG through both exchange dilution and the modification of sublattice magnetizations.[28,32]

2. Structural, Magnetic, and Stoichiometric Analysis

We analyze the sublattice occupancy in both thin-film and bulk TbIG through a combination of experimental techniques and modeling. The bulk sample is produced by powder processing and the 40 to 60 nm thick (111)-oriented films by PLD (see Experimental Section). The Fe site occupancies of bulk and thin-film TbIG are obtained by fitting X-ray magnetic circular dichroism (XMCD) data with a relativistic Hartree–Fock model augmented by crystal field theory, and this data is input into a molecular field model to yield a site occupancy model that is consistent with the measured composition and T_{comp}. Direct evidence of the existence of Tb antisite defects is provided by high-angle annular dark field scanning transmission electron microscopy (HAADF-STEM) imaging and energy dispersive X-ray spectroscopy (EDS).

A high-resolution X-ray diffraction (HRXRD, Bruker Discover D8) 2θ-ω spectrum about the (444) reflection of a 52 nm-thick TbIG thin film sample and a powder diffraction (Philips X'Pert Pro) 2θ-ω spectrum from the bulk TbIG sample are presented in Figure 1a,b. For the bulk TbIG, all peaks in the powder XRD spectrum can be attributed to garnet. A Rietveld refinement was performed on this spectrum by fitting to the iron site occupancies, using a least-squares fit of the powder XRD spectrum to extract fractional atomic coordinates, site occupancies, and other structural parameters.[45] The best-fit yields a 2:3 Fe_{oct}:Fe_{tet} ratio within a 1% uncertainty, justifying the use of the bulk sample as a reference in subsequent analyses. The HRXRD spectrum of the thin film displayed Laue fringes, indicating good thickness uniformity. A reciprocal space map (RSM) around the (642) diffraction peak from a pre-

16136829, 0, Downloaded from https://onlinelibrary.wiley.com/doi/10.1002/smll.202300824 by Massachusetts Institute of Technolo, Wiley Online Library on [15/04/2023]. See the Terms and Conditions (https://onlinelibrary.wiley.com/terms-and-conditions) on Wiley Online Library for rules of use; OA articles are governed by the applicable Creative Commons License

16136829, 0, Downloaded from https://onlinelibrary.wiley.com/doi/10.1002/smll.202300824 by Massachusetts Institute of Technolo, Wiley Online Library on [15/04/2023]. See the Terms and Conditions (https://onlinelibrary.wiley.com/terms-and-conditions) on Wiley Online Library for rules of use; OA articles are governed by the applicable Creative Commons License

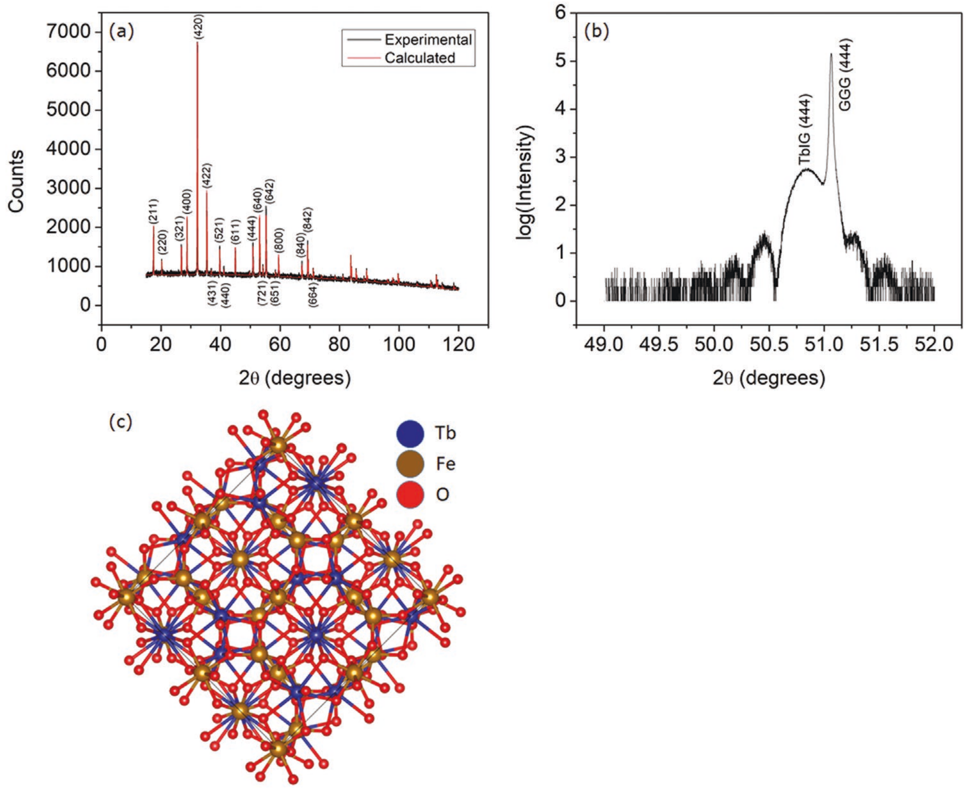

Figure 1. Structural characterization of TbIG bulk and thin film samples. a) Powder diffraction scan of the TbIG bulk sample. The calculated spectrum was fit using Rietveld refinement. b) HRXRD scan of the (444) reflection of a TbIG thin film sample. c) (111) projection of the TbIG unit cell (element colors are listed in the legend).

viously reported TbIG film grown under the same conditions[19] indicates a coherent interface between the TbIG and the GGG substrate, with the epitaxial TbIG in a state of in-plane compressive strain due to lattice mismatch with the GGG.

The TbIG film is richer in Tb than the target composition, which is attributed to differential scattering between the Tb and Fe in the PLD plume during the growth process.[46] This is a common phenomenon in PLD-grown garnet films.[19,28,31,32] In our prior work, we reported a Tb:Fe ratio of 0.70 for the film from X-ray photoelectron spectroscopy (XPS) measurements using the relative sensitivity factor library native to the instrument.[19] To improve the accuracy of the composition measurement for the quantitative work in this study, we performed an XPS (Physical Electronics Versaprobe II) survey and high-resolution scans of both the thin-film and bulk samples (**Figure 2**a) and used the bulk sample as a calibration standard with a composition of Tb:Fe = 0.60 (see Supporting Information for more details). This yielded a composition of Tb:Fe = 0.86 ± 0.05 for the thin-film sample, confirming the presence of excess Tb. Prior to collecting the XPS survey scans, in situ ion milling was used to remove carbon contamination from the surface. After ion milling, the C 1s peaks (which overlap with Tb 4p3/2) of the spectra shown in Figure 2 only differ by ≈3%. This implies that the effect of carbon contamination on the quantification is likely to be minimal, especially after normalization.

Temperature-dependent vibrating sample magnetometry (VSM, DMS 880) measurements of hysteresis loops in the range of 230–540 K were performed to determine the saturation magnetization of the thin film and bulk TbIG samples, and their T_{comp} and T_{Curie}. Representative room-temperature hysteresis loops from both bulk and film samples are provided in Figure 2b. For the film, the field was applied along the easy axis, perpendicular to the plane; the perpendicular magnetic anisotropy is dominated by magnetoelastic anisotropy arising from the positive magnetostriction coefficient λ_{111} and the in-plane compressive strain, though a growth-induced anisotropy likely also contributes.[21] However, for the TbIG thin film samples, the magnitude of the perpendicular anisotropy energy proved difficult to extract. This is due to the large and nonlinear background of the GGG substrate which overwhelms the comparatively small signal from the film.[19,21] Our group's prior work on similar films suggests that the anisotropy field is in excess of 150 mT.[32]

From Figure 2c, the T_{comp} of the bulk TbIG sample was 240 ±10 K, which is consistent with a reported bulk value of 248.6 K.[19] The coercive field diverges as the temperature approaches T_{comp} as shown in our prior work.[19] However, the T_{comp} of the thin film was considerably higher, at 330 ±10 K.[19] T_{Curie} (the temperature at which the material becomes paramagnetic, defined here as the temperature at which the hysteresis loop amplitude lies within the noise of the VSM, Figure 2d) was ≈40 K lower for the film compared to the bulk sample. This suggests the presence of vacancies within the film, which are known to lower T_{Curie} through exchange dilution.[2] The changes in T_{comp} and T_{Curie} for the film are unlikely to be a result of strain-induced modulation of the exchange coefficients because an ab initio theoretical study of strained GdIG predicted that both T_{comp} and T_{Curie} should increase with in-plane compressive

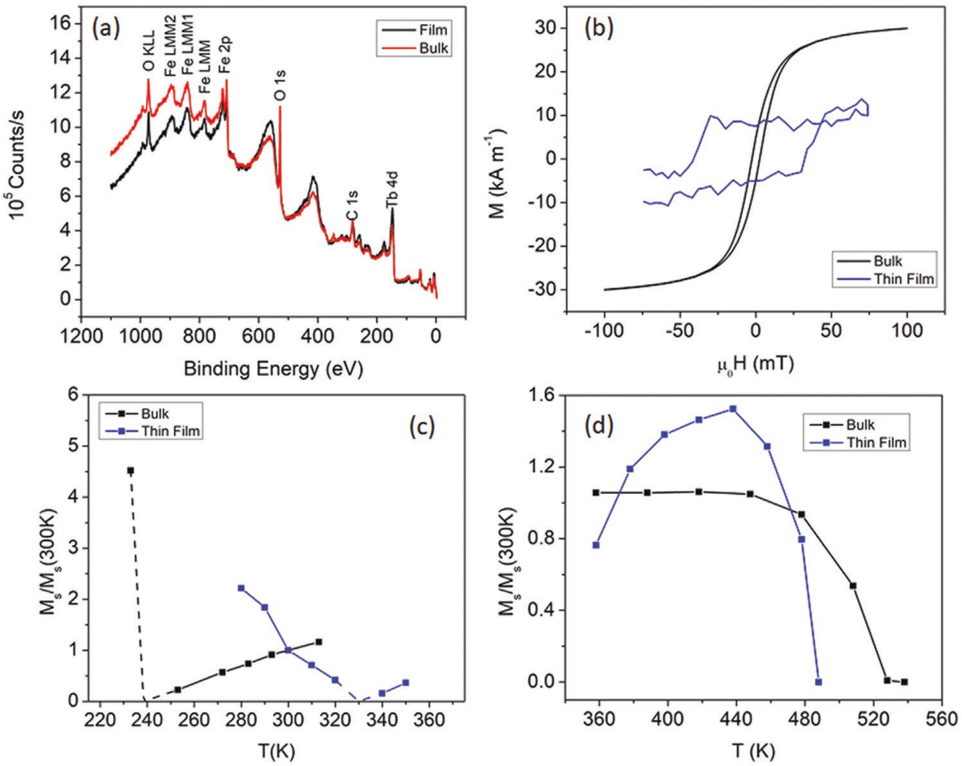

Figure 2. a) XPS survey spectra of TbIG thin film and bulk samples used for stoichiometric analysis. The main peaks in the spectra are labeled. b) Room-temperature VSM hysteresis loops of TbIG thin film and bulk samples (thin film data reproduced from Rosenberg et al. 2018).[19] Temperature-dependent magnetometry of TbIG thin film and bulk samples. c) Low-temperature scan revealing the higher-than-bulk compensation temperature of the TbIG thin film sample. d) High-temperature scan revealing the lower-than-bulk Curie temperature of the TbIG thin film sample.

strain.[47] Therefore, we now turn to the investigation of the role of site occupancies to explain the differences between the thin film and bulk TbIG.

3. Extraction of Iron Site Occupancies and Terbium Valence via X-Ray Core-Level Spectroscopy

We use XMCD to extract the site occupancies of the Fe ions based on the Hartree–Fock model initially proposed by R. C. Cowan to predict the energy levels and emission spectra of isolated atoms.[48] The model was augmented by T. Thole[49] with Butler's group theory formalism[50] so that it could be used to calculate the X-ray absorption spectra (XAS) of ions in coordinated lattice sites and in an exchange field. This software package, which in its current form is known as CTM4XAS,[51] is able to calculate the XAS and XMCD spectra of transition metals with site and magnetic sublattice specificity, for example, to quantify iron valence and site occupancies extracted from magnetite and cobalt ferrite spinels.[52–54] The Fe XMCD L edge contains three main peaks which can be uniquely mapped back to the spectral fingerprints of different Fe species such as Fe^{3+}_{oct}, Fe^{2+}_{oct}, and Fe^{3+}_{tet}. By adding these component spectra together, a linear combination fit to an experimental spectrum can be accomplished through the method of nonlinear least squares.

Circularly polarized XAS data in total electron yield (TEY) mode from the bulk and thin-film TbIG samples were collected at the 4-ID-C beamline at the Advanced Photon Source at Argonne National Laboratory and are displayed in **Figure 3**a. The data were shifted to match an internal Fe foil reference so that the energy scales for the bulk and thin film data agree. The XAS data were normalized using Athena[55] and the left- and right-hand circular polarization (LHCP and RHCP) spectra from data collected at remanence from positive and negative fields were subtracted using the formula

$$\mathrm{XMCD} = \frac{(\sigma_{\downarrow\uparrow} + \sigma_{\uparrow\downarrow}) - (\sigma_{\uparrow\uparrow} + \sigma_{\downarrow\downarrow})}{2} \tag{1}$$

in order to eliminate any nonmagnetic artifacts (Figure 3b–d). In Equation (1), σ_{ij} is the data collected with the ith polarization and the jth magnetic field direction. The data were then fitted using a custom Python interface to CTM4XAS. The experimental XMCD L3-edge XMCD spectrum (between ≈705 and 713 eV) was fit using nonlinear least squares to the expression

$$\mathrm{XMCD}_{\mathrm{exp}} = a\left(f_1 \mathrm{XMCD}_{\mathrm{Fe^{3+}Oh}} + f_2 \mathrm{XMCD}_{\mathrm{Fe^{3+}Td}} + f_3 \mathrm{XMCD}_{\mathrm{Fe^{2+}Oh}}\right) \tag{2}$$

where a is an overall scaling parameter, f_i is the fraction of the ith spectral component, $\mathrm{XMCD}_{\mathrm{exp}}$ is the experimental XMCD spectrum, and $\mathrm{XMCD}_{\mathrm{Fe}^{3+}\mathrm{Oh}}$ (for example) is the simulated XMCD spectrum, calculated using the TT-Multiplets interface to the Cowan Hartree–Fock codes, for Fe^{3+} occupying an octahedral site. The f_i is not necessarily the exact site occupancies of the Fe ions but can be determined quantitatively by comparison with data from the bulk TbIG sample which has a 2:3 octahedral:tetrahedral Fe ratio according to the Rietveld refinement.

© 2023 Wiley-VCH GmbH

16136829, 0, Downloaded from https://onlinelibrary.wiley.com/doi/10.1002/smll.202300824 by Massachusetts Institute of Technolo, Wiley Online Library on [15/04/2023]. See the Terms and Conditions (https://onlinelibrary.wiley.com/terms-and-conditions) on Wiley Online Library for rules of use; OA articles are governed by the applicable Creative Commons License

16136829, 0, Downloaded from https://onlinelibrary.wiley.com/doi/10.1002/smll.202300824 by Massachusetts Institute of Technolo, Wiley Online Library on [15/04/2023]. See the Terms and Conditions (https://onlinelibrary.wiley.com/terms-and-conditions) on Wiley Online Library for rules of use; OA articles are governed by the applicable Creative Commons License

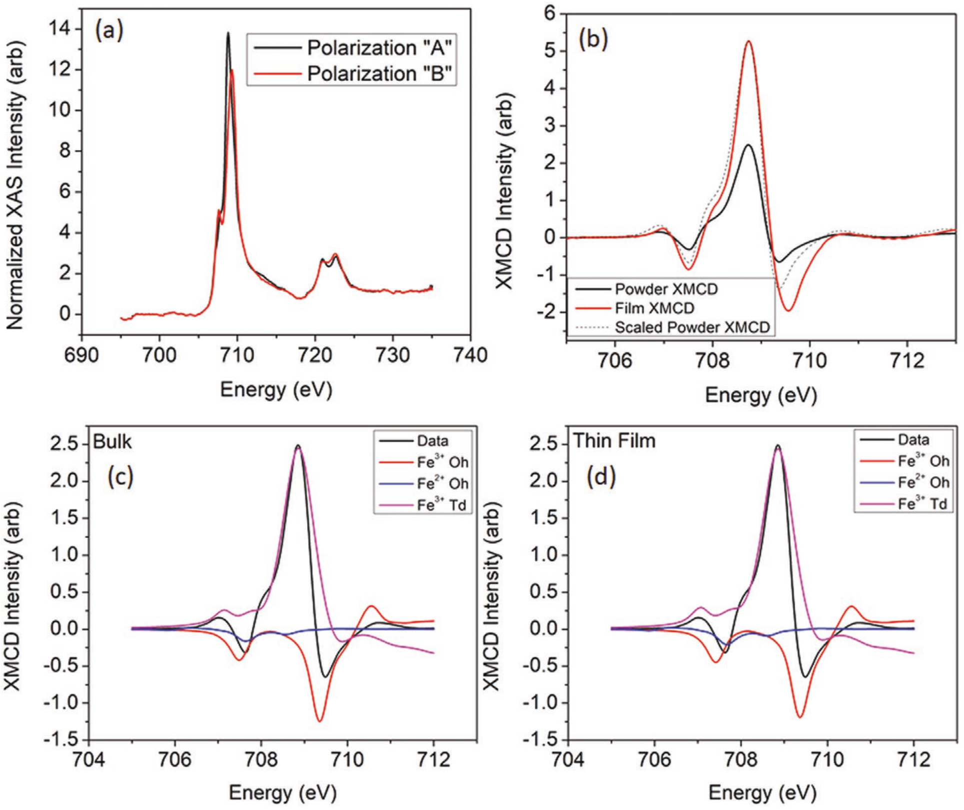

Figure 3. Fe L-edge spectra. a) LHCP and RHCP (polarizations A and B) XAS spectra showing polarization contrast. b) XMCD spectra calculated according to Equation (2) in the main text. The powder (bulk) spectrum was scaled to lie on the same axes as the thin film spectrum. c,d) XMCD spectra from bulk (c) and thin film (d) TbIG samples, fit with Hartree–Fock simulations as described in the text. The best fits of each component (Fe^{3+} Oh, Fe^{3+} Td, and Fe^{2+} Oh) are displayed along with the experimental spectra.

The important fitting parameters are the Gaussian and Lorentzian broadening, the chemical shifts, the crystal field, the Slater Integral reduction, and the exchange energy. The Gaussian broadening is due to the energy resolution of the beamline, which is 0.1 eV for 4-ID-C. The Lorentzian broadening is somewhat more complex, as it is due to fundamental relaxation processes (core-hole lifetime) in the material.[56] Some groups have noted that an energy-dependent broadening may be appropriate,[57] while others use a constant value for the entire L3 edge.[58] We use the latter method (constant broadening of 0.2 eV) so as not to overfit the data. The chemical shifts between the octahedral and tetrahedral spectra depend on the valence, site symmetry, and crystal structure, and were determined during the fitting process.

The crystal field is the Coulomb interaction due to the oxygen ions coordinated to the Fe ion in question. In TbIG, the two crystal field symmetries (octahedral (Oh) and tetrahedral (Td)) are parametrized by the crystal field parameter, 10Dq(oct)/10Dq(tet), respectively. An octahedral or tetrahedral crystal field causes the five Fe 3d states to split into a doublet (E symmetry) and a triplet (T2 symmetry), and the energy between these two degenerate sets is 10Dq, positive for Oh and negative for Td.[2] Where the bond lengths between the two types of polyhedra are identical, 10Dq(oct)/10Dq(tet) = –9/4,[59] but in garnets, this is not a good approximation.[59] Rough values of 10Dq were therefore extracted from ref. [60] and improved by least squares fitting. The exact values of 10Dq are not crucial, as the spectral shape varies slowly with 10Dq.

Cowan's approach calculates spectra for isolated ions (that is, systems with perfectly flat bands), and Slater integrals[61] are included to describe direct and exchange interactions between electrons. For instance, in a $1s^1 2s^1$ configuration, the Coulomb energy of the ^1S configuration is $<^1S|e^2/\mathbf{r}_{12}|^1S> = F^0(1s2s) + G^0(1s2s)$ where F^0 and G^0 are the direct and exchange Slater integrals. When the atoms are embedded in a coordination structure, the overall effect is to reduce the Slater integrals. We used values F_{dd}, F_{pd}, and G_{pd} from a study on Ce:YIG, and then further optimized them to fit our data.[58] A final non-essential fitting parameter is the exchange energy which was included as an additional symmetry breaking to allow the simulation of the XMCD. If the simulations are carried out at elevated temperatures, the exchange energy value affects the lineshape, but here all simulations were carried out at 0 K.

The fitting parameter values are displayed in **Table 1** and the fitted curves obtained with these values are displayed in Figure 3c,d. With this choice of parameters, the thin film and bulk site occupancies were extracted (**Table 2**). During the fitting process, the ratio of 3d holes for Fe^{3+} and Fe^{2+} (5:4) was used to normalize the areas of the simulated XAS spectra. The results indicate that the TbIG thin film has an Oh:Td ratio that is about 10% greater than that of the bulk sample, that is, there is a slightly lower concentration of non-Fe species (vacancies or

Table 1. Fitting parameters used in Hartree–Fock simulations of TbIG thin film and bulk samples.

Parameter	Value	Source
10Dq [Fe^{3+}_{oct}] (eV)	1.8 (thin film), 1.7 (bulk)	Fitting
10Dq [Fe^{3+}_{tet}] (eV)	−0.8 (thin film), −0.7 (bulk)	Fitting
10Dq [Fe^{2+}_{oct}] (eV)	1	Fitting
Chemical shift (Fe^{2+}_{oct}-Fe^{3+}_{oct}) (eV)	0.85 (thin film), 0.92 (bulk)	Fitting
Chemical shift (Fe^{2+}_{oct}-Fe^{3+}_{tet}) (eV)	0.93 (thin film), 0.99 (bulk)	Fitting
M [Fe_{oct}] (meV)	−12	Vasili et al.[58]
M [Fe_{tet}] (meV)	18	Vasili et al.[58]
F_{dd} (eV)	0.75 [Oh], 0.65 [Td]	Vasili et al.[58] and Fitting
F_{pd} (unitless)	0.85	Vasili et al.[58] and Fitting
G_{pd} (unitless)	0.825	Vasili et al.[58] and Fitting

10Dq is the crystal field energy and M is the magnetic exchange energy. F_{dd}, F_{pd}, and G_{pd} are Slater integral scaling factors. For instance, F_{pd} of 0.85 corresponds to 5.063 eV for Fe^{3+}_{oct}.

Table 2. Best-fit site occupancies of TbIG thin film and bulk samples, extracted via TT-Multiplets fitting.

Species	TbIG thin film	TbIG bulk
Fe^{3+} Oh	0.29	0.28
Fe^{3+} Td	0.66	0.68
Fe^{2+} Oh	0.05	0.04
Oh:Td Ratio	0.73 (0.52)	0.66 (0.47)

The bottom row is the corrected Oh:Td ratio taking into account the 2:3 ratio of bulk TbIG (the raw values are in parentheses).

antisite defects) on the octahedral sites compared to the tetrahedral. Therefore, iron-site vacancies are expected, which must be present on both sites based on the octahedral/tetrahedral occupancy ratio of Fe. This provides an explanation for the Curie temperature reduction observed in Figure 2d, consistent with the mechanism of exchange dilution within the thin film.[2,62]

Unlike transition metals, XMCD is not well-suited to the elucidation of rare-earth coordination numbers. However, XAS can still be used to identify the valence states of the terbium ions present in our TbIG samples. XAS and XMCD spectra were collected at the Tb $M_{4,5}$ edge using a similar procedure to that used for the Fe $L_{2,3}$ edge. In **Figure 4**a, we plot representative normalized spectra taken from the thin film sample.[63] By comparing with calculated and experimental literature spectra, the spectral features can be explained solely by a Tb^{3+} contribution.[63,64] This can also be seen from the Tb 4d XPS spectrum (Figure 4b). Note that in our past work,[19,32,65] we attributed certain features of the Tb 3d and 4d XPS spectra to contributions from Tb^{4+}. This was derived from the peak assignments made in prior work on Tb-containing compounds.[66–68] However, the features in these spectra can also be completely explained by Tb^{3+}.[69] In the following discussion, we will assume that all of the Tb is in the 3+ state, in accordance with our XAS results.

4. Direct Evidence of Terbium Antisite Defects

The excess Tb may be accommodated as Tb antisite defects or via Fe vacancies. The existence of rare-earth antisites in garnet crystals has been established for yttrium aluminum garnet (YAG) or terbium scandium aluminum garnet (TSAG) compositions, such as Er:YAG, in which both Er^{3+} and Y^{3+} substitute for octahedral iron,[70] and (Y,Lu):TSAG, in which Y^{3+} and Lu^{3+} dopants substitute for octahedral iron.[71] We expect antisite defects to be present due to the large Tb fraction in our thin films, but cation disorder has not yet been studied for TbIG. Here, we provide direct evidence of terbium antisite defects in TbIG via STEM-EDS measurements.

A plan view TEM sample of the TbIG/(111)GGG thin film was prepared via mechanical polishing and Ar^+ ion milling. **Figure 5**a depicts the atomic resolution HAADF-STEM image and EDS elemental maps of Tb and Fe along the [111] projection, normal to the film plane. Along this zone axis, the columns of dodecahedral, octahedral, and tetrahedral sites are separately visible. We use the non-overlapping Tb M and Fe L peaks in the X-ray spectrum to obtain the EDS elemental maps in Figure 5. The Tb elemental map shows evidence of Tb present in the octahedral Fe atomic columns as marked by arrows. From the EDS intensity, a larger amount of Tb antisites

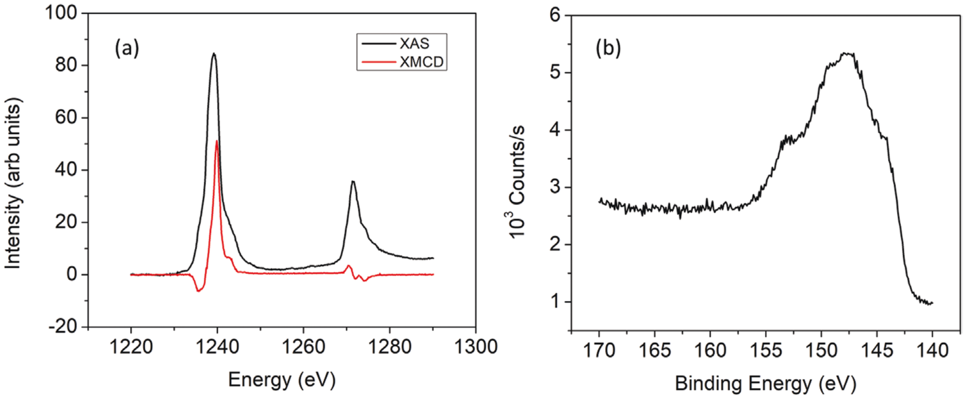

Figure 4. Tb $M_{4,5}$ edge XAS and XMCD spectra (XMCD scaled to lie on same axes as XAS) (a) and $4d_{2,3}$ high-resolution XPS spectrum (b) from a representative TbIG thin film. Both of these spectra are highly consistent with the presence of only Tb^{3+} species within the film.

© 2023 Wiley-VCH GmbH

16136829, 0, Downloaded from https://onlinelibrary.wiley.com/doi/10.1002/smll.202300824 by Massachusetts Institute of Technolo, Wiley Online Library on [15/04/2023]. See the Terms and Conditions (https://onlinelibrary.wiley.com/terms-and-conditions) on Wiley Online Library for rules of use; OA articles are governed by the applicable Creative Commons License

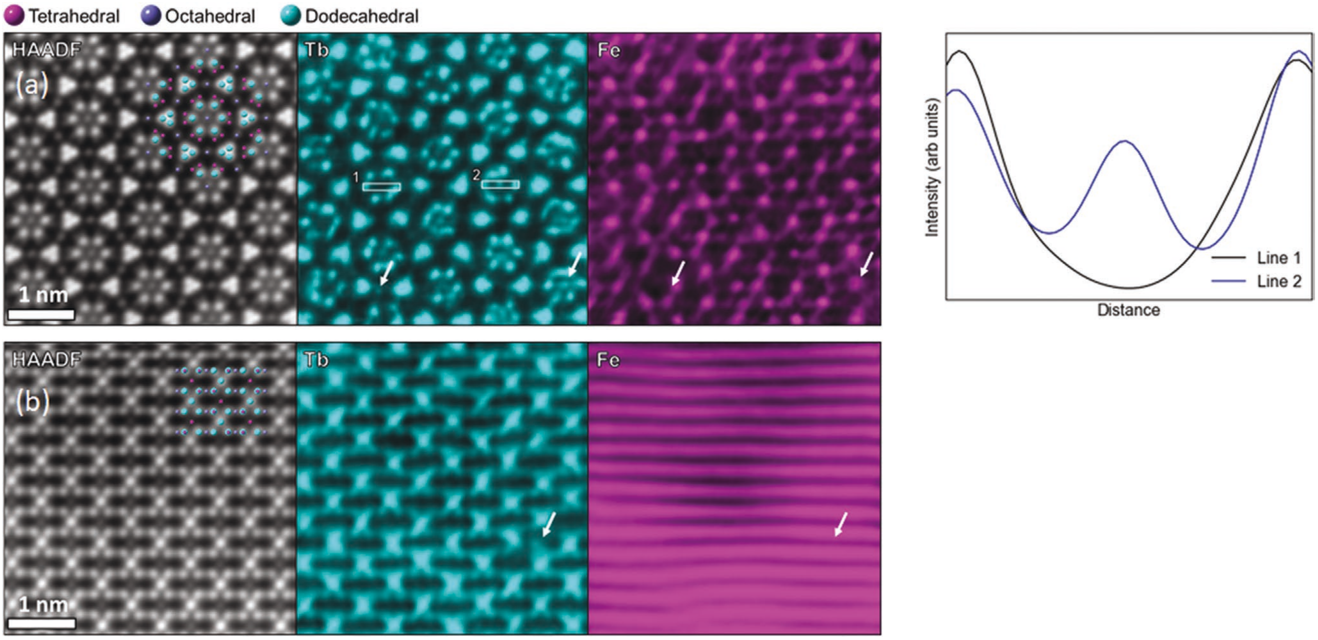

Figure 5. Atomic resolution HAADF STEM images and STEM EDS elemental mappings of Tb and Fe, viewed along [111] zone axis (a) and [110] zone axis (b). Arrows indicate the location of Tb antisites. The legend at the top identifies the sites in the crystal models superposed on the HAADF images. The intensity profiles in the rightmost panel of (a) show the contrast seen when antisite defects are present (Line 1) versus absent (Line 2).

are found to occupy the octahedral sites in the center of six Tb atom columns as compared to the octahedral sites in between three Tb columns. However, identification of Tb antisites in tetrahedral sites is less straightforward in the [111] projection, because the tetrahedral Fe atomic columns appear close to the neighboring Tb atomic columns. To investigate the presence of tetrahedral Tb antisites, we tilted the sample to align the beam along a [110] zone axis. STEM-EDS measurements performed along the [110] projection reveal the occupation of Tb in one of the tetrahedral Fe columns marked by an arrow in Figure 5b. These results clearly indicate that Tb preferentially occupies the octahedral atomic sites versus the tetrahedral sites, as expected from the larger size of the octahedral interstice.

5. Molecular Field Analysis of TbIG Incorporating Point Defects

In order to analyze the effect of the point defects (both Fe vacancies and Tb antisites) on T_{comp}, molecular field simulations were carried out following the formalism developed by Dionne,[2,32,72,73] treating Fe^{3+} vacancies as diamagnetic substitutions. We consider the effect of both Fe vacancies and octahedral Tb antisite defects. XMCD cannot distinguish between octahedrally and dodecahedrally coordinated terbium ions due to lifetime broadening and the screening of rare-earth core electrons from the crystal field,[63] so the XMCD data does not show what fraction of the excess Tb ions occupy the octahedral sites. For Tb^{3+} present on dodecahedral sites, the molecular field coefficients, the g factor, and the total angular momentum J of Tb^{3+} were used, but for octahedral Tb^{3+} ions, the molecular field coefficients of octahedral Fe^{3+} were used due to the shorter bond lengths, while retaining g and J of Tb^{3+}. In essence, the lattice site symmetry is assumed to have a greater effect on the molecular field coefficient than the species or valence state.

The Tb:Fe ratio was varied by initially introducing Fe vacancies. These were placed on the octahedral and tetrahedral sites in 2:3 proportion in the molecular field simulation, maintaining the Fe_{oct}:Fe_{tet} ratio determined from the Rietveld refinement and XMCD fitting. To account for Tb antisites, Tb^{3+} was placed in the octahedral sites, replacing the octahedral vacancies in a proportion of 0%, 15%, 25%, and 50%, thereby ensuring that the non-Fe species on these sites, that is, Fe vacancies and Tb antisite defects, maintain a 2:3 proportion. The predicted T_{comp} from these simulations is shown in **Figure 6**. At the stoichiometric composition of Tb:Fe = 0.6, all of the T_{comp} curves converge at the bulk compensation temperature of 250 K, as expected for TbIG with no vacancies or antisite defects. This serves as a positive check on the validity of our calculations.

It is apparent from the simulations with 0% Tb antisite defects that iron vacancies alone are not enough to raise T_{comp} to the observed value of 335 K. At the actual film composition of Tb:Fe = 0.86, the calculated T_{comp} is only 296 K, that is, there must also be antisite Tb present. As Tb^{3+} has a higher moment than Fe^{3+}, Tb^{3+} octahedral antisite defects increase the moment of the octahedral sublattice and raise T_{comp}. When 15% of the octahedral Fe^{3+} vacancies are filled with Tb^{3+} antisite defects (Figure 6), both the observed Tb:Fe ratio of 0.86 and T_{comp} of 335 K are well matched by the model. It is also important to note that this model only uses a single fitting parameter: the percentage of Tb antisite defects. The other inputs to the model are the balance between the octahedral and tetrahedral Fe vacancies (supplied by XMCD fitting), the composition (supplied by XPS), and the antisite molecular field coefficients (discussed previously). Changing these parameters would somewhat alter our result of 15% Tb antisites, but the direct

16136829, 0, Downloaded from https://onlinelibrary.wiley.com/doi/10.1002/smll.202300824 by Massachusetts Institute of Technolo, Wiley Online Library on [15/04/2023]. See the Terms and Conditions (https://onlinelibrary.wiley.com/terms-and-conditions) on Wiley Online Library for rules of use; OA articles are governed by the applicable Creative Commons License

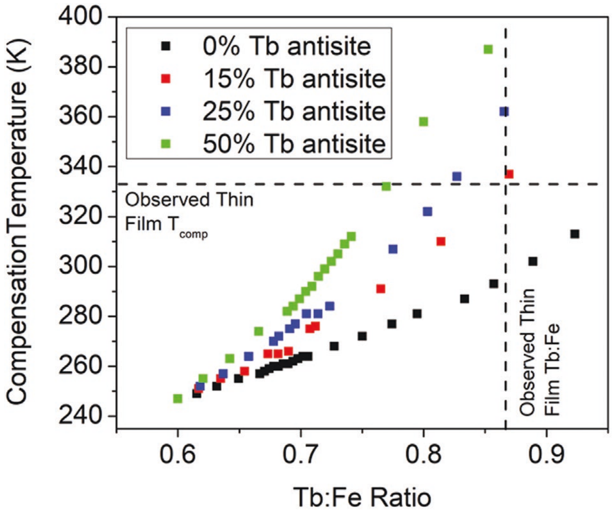

Figure 6. TbIG compensation temperatures calculated by molecular field simulations as a function of Tb:Fe ratio. Each point represents the result of a single molecular field simulation, and the different colors correspond to simulations run with different fractions of octahedral vacancies filled with Tb antisite defects. The intersection of the dotted lines is the experimentally observed compensation temperature at the Tb:Fe ratio of our TbIG thin film.

detection of the antisites via TEM, as well as the fact that the black 0% antisite curve is able to reproduce the bulk T_{comp} but not the film T_{comp} are two strong arguments in favor of our-model. As an additional check, we also investigated simpler models (e.g. neglecting vacancies) but found them lacking in explanatory power (see Supporting Information).

We can then derive an empirical chemical formula for our PLD-grown TbIG thin films in a four-step process by starting with a general formula and iteratively introducing constraints from the XPS, XMCD, and molecular field simulation results. The general formula for TbIG is taken as

$$\left\{\mathrm{Tb}_3^{3+}\right\}\left[\mathrm{Fe}_{2-a-b-c}^{3+}\mathrm{Fe}_a^{2+}\mathrm{V}_b\mathrm{Tb}_c^{3+}\right]\left(\mathrm{Fe}_{3-d}^{3+}\mathrm{V}_d\right)\mathrm{O}_{12-\delta}^{2-} \tag{3}$$

where {}, [], and () represent dodecahedral, octahedral, and tetrahedral coordination respectively, V_i represents vacancies on the i site, and δ represents oxygen deficiency. Without an independent measurement of XMCD for a bulk TbIG sample with a known amount of Fe^{2+}, we cannot accurately quantify the fraction of Fe^{2+} in the thin film. However, we know that the proportion of Fe^{2+} must be small because the spectral component is very weak (about 5% of the total peak area) compared to published spinel spectra with a large Fe^{2+} contribution,[54] so we are justified in assuming that all of the iron is in the 3+ state and setting $a = 0$. The following three constraints are then solved for the remaining three variables, b, c, and d

$$\frac{3+c}{5-b-c-d} = 0.86 \text{ (Tb : Fe ratio from XPS)} \tag{4}$$

$$\frac{2-b-c}{3-d} = 0.602 \text{ (}\mathrm{Fe_{oct}} : \mathrm{Fe_{tet}}\text{ ratio from XMCD)} \tag{5}$$

$$\frac{c}{b+c} = 0.15 \text{ (Tb antisite defects as a fraction of octahedral defects from MFC model)} \tag{6}$$

By solving these three equations, we arrive at the following chemical formula

$$\left\{\mathrm{Tb}_3^{3+}\right\}\left[\mathrm{Fe}_{1.35}\mathrm{V}_{0.55}\mathrm{Tb}_{0.097}^{3+}\right]\left(\mathrm{Fe}_{2.25}^{3+}\mathrm{V}_{0.75}\right)\mathrm{O}_{12-\delta}^{2-} \tag{7}$$

These defect concentrations are much higher than those observed by Manuilov et al. for PLD-grown YIG, for which the amounts of non-Fe species $b + c$ and d were found to equal 0.19 and 0.13, respectively.[31] Su et al. achieved comparable defect concentrations in PLD-grown Y-rich YIG (i.e., $Y_3YFe_4O_{12}$) with $b + c$ and d values of 0.7 and 0.99, respectively.[62]

Finally, we address the issue of charge neutrality. If all of the charged defects (vacancies) are added up, the net charge is 3.9 per formula unit. This could be compensated with $\delta = 1.95$ oxygen vacancies per 12 O ions in the above formula, representing an upper bound as we have neglected the existence of Fe^{2+}. Another possibility is the existence of charged vacancies, but an ab initio study[74] of defects in YIG has shown that vacancies in garnet systems act more like acceptors than donors. Therefore, positively charged vacancies contributing to charge neutrality seem unlikely. A technique more sensitive to point defects, such as resonant X-ray diffraction or EXAFS, could address this question in more depth.

6. Conclusion

This study shows that in a complex oxide, TbIG, a considerable amount of excess Tb (Tb:Fe = 0.86, compared to 0.6 in stoichiometric $Tb_3Fe_5O_{12}$) can be incorporated in films grown epitaxially on a garnet substrate. From analysis based on a combination of STEM, XPS, Rietveld refinement, a Hartree–Fock analysis of XMCD data, and a molecular field model of magnetization versus temperature, we find that the excess Tb is accommodated by octahedral Tb antisite defects and by vacancies on both octahedral and tetrahedral sites. The analysis is consistent with predominantly trivalent Tb and Fe cations, with a minor amount of divalent Fe. We apply all of the experimentally-derived constraints on the chemical species in order to derive an empirical chemical formula for the PLD-grown TbIG thin films. Using STEM, we obtain direct confirmation of the existence of octahedral Tb antisite defects within the thin film, despite the large ionic radius of the Tb^{3+}.

The compensation temperature proves to be a sensitive measure of defect populations, and the presence of several types of point defects likely explains the discrepancies between compensation temperatures found in many reports of REIG thin films versus bulk values.[18,19,22,39,40] The stabilization of large defect populations in epitaxial films has important implications for the design of REIGs for spintronic applications and more generally for the engineering of complex oxide films for electronics and other applications. Defect engineering through co-deposition or control of growth parameters, therefore, emerges as a powerful method to control the magnetic properties of REIGs. The analysis of defect populations via magnetic

16136829, 0, Downloaded from https://onlinelibrary.wiley.com/doi/10.1002/smll.202300824 by Massachusetts Institute of Technolo, Wiley Online Library on [15/04/2023]. See the Terms and Conditions (https://onlinelibrary.wiley.com/terms-and-conditions) on Wiley Online Library for rules of use; OA articles are governed by the applicable Creative Commons License

and structural characterization may be generalized to a range of ferrimagnetic garnets and other oxides.

7. Experimental Section

Bulk and Thin Film Preparation: Polycrystalline TbIG samples were fabricated by mixing Fe_2O_3 and Tb_4O_7 powders in a 6:1 stoichiometric ratio with a ball mill, calcining the green body at 1150 °C for 5 h, re-grinding the powders, and sintering at 1350 °C for 10 h.[19] Pieces of this sample were ground up in a mortar and pestle to produce TbIG powder for powder diffraction measurements. Thin-film samples of thickness 40 nm (for XMCD and XPS) and 52 nm (for Curie temperature measurements) were prepared on (111) GGG substrates by pulsed laser ablation of a target of the bulk material using a 248 nm wavelength Compex Pro laser operated at 400 mJ per pulse ($\approx$2 mJ cm^{-2}), a repetition rate of 10 Hz, a substrate-target distance of 8 cm, a substrate heater temperature of 900 °C corresponding to a sample temperature of $\approx$750 °C, and an O_2 pressure of 150 mTorr. After the growth process, the films were cooled at a rate of 10 °C min^{-1} in 150 mTorr of O_2.

Thin Film and Bulk Characterization: High-resolution XRD 2θ-ω and XRR scans were carried out with a Bruker D8 Discover diffractometer. Powder XRD scans were performed with a Philips X'pert Pro diffractometer and Rietveld refinement was carried out with Panalytical Highscore Plus. All VSM hysteresis loops were collected in a DMS 880A VSM. XPS survey and high-resolution scans were collected in a Physical Electronics Versaprobe II spectrometer.

XAS and XMCD Measurements: Spectra were collected in TEY mode at the 4-ID-C beamline of the Advanced Photon Source at Argonne National Laboratory. All spectra were collected at 200 K. Fitting of the Fe data was accomplished using a custom Python interface to the RCG-RAC-BAN codes with input file templates generated with CTM4XAS.

HAADF-STEM Measurements: The plan view sample of TbIG was prepared via mechanical wedge polishing and was further thinned by Ar+ ion milling using a Fischione 1051 mill. STEM imaging and EDS measurements were performed with a probe-corrected Thermo Fisher Scientific Themis-Z G3 60–300 kV microscope operated at 200 kV. The collection semi-angle range was 65–200 mrad for HAADF imaging with a convergence angle of 18 mrad. The presence of Tb in the octahedral Fe site was visible in the raw Tb map without further processing. Tb and Fe elemental maps were denoised with nonlocal principal component analysis[75] and Gaussian blurring.

Supporting Information

Supporting Information is available from the Wiley Online Library or from the author.

Acknowledgements

The authors acknowledge support from the National Science Foundation awards 1419807, 1808190, and 2128199, and from SMART, an nCORE Center supported by SRC and NIST. Shared facilities of the MRSEC under award NSF 1419807 were used. Work at the Advanced Photon Source was supported by the U.S. Department of Energy, Basic Energy Sciences under Grant no. D-EAC02-06CH11357.

Conflict of Interest

The authors declare no conflict of interest.

Data Availability Statement

The data that support the findings of this study are available from the corresponding author upon reasonable request.

Keywords

complex oxides, defect engineering, epitaxial stabilization, garnets, magnetic thin films

Received: February 16, 2023
Published online:

---

[1] B. Keimer, S. A. Kivelson, M. R. Norman, S. Uchida, J. Zaanen, *Nature* **2015**, *518*, 179.
[2] G. F. Dionne, *Magnetic Oxides*, Springer Science+Business Media, Springer, New York **2009**.
[3] M. Dawber, K. M. Rabe, J. F. Scott, *Rev. Mod. Phys.* **2005**, *77*, 1083.
[4] Y.-T. Chen, S. Takahashi, H. Nakayama, M. Althammer, S. T. B. Goennenwein, E. Saitoh, G. E. W. Bauer, *Phys. Rev. B* **2013**, *87*, 144411.
[5] A. P. Ramirez, *J. Phys. Condens. Matter* **1997**, *9*, 8171.
[6] M. Imada, A. Fujimori, Y. Tokura, *Rev. Mod. Phys.* **1998**, *70*, 1039.
[7] S. D. Tilley, M. Cornuz, K. Sivula, M. Grätzel, *Angew. Chem., Int. Ed.* **2010**, *49*, 6405.
[8] F. S. Stone, *J. Solid State Chem.* **1975**, *12*, 271.
[9] V. Thangadurai, S. Narayanan, D. Pinzaru, *Chem. Soc. Rev.* **2014**, *43*, 4714.
[10] D. B. Roth, M. Gellert, *Nature* **2000**, *404*, 821.
[11] S. Ning, A. Kumar, K. Klyukin, E. Cho, J. H. Kim, T. Su, H. S. Kim, J. M. LeBeau, B. Yildiz, C. A. Ross, *Nat. Commun.* **2021**, *12*, 4298.
[12] H. L. Tuller, S. R. Bishop, *Annu. Rev. Mater. Res.* **2011**, *41*, 369.
[13] W. Li, J. Shi, K. H. L. Zhang, J. L. Macmanus-Driscoll, *Mater. Horiz.* **2020**, *7*, 2832.
[14] V. Zviagin, M. Grundmann, R. Schmidt-Grund, *Phys. Status Solidi* **2020**, *257*, 1900630.
[15] Y. Sun, J. Yang, S. Li, D. Wang, *Chem. Commun.* **2021**, *57*, 8402.
[16] D. J. Keeble, R. A. MacKie, W. Egger, B. Löwe, P. Pikart, C. Hugenschmidt, T. J. Jackson, *Phys. Rev. B: Condens. Matter Mater. Phys.* **2010**, *81*, 064102.
[17] A. Catellani, A. Ruini, A. Calzolari, *J. Mater. Chem. C* **2015**, *3*, 8419.
[18] A. Quindeau, C. O. Avci, W. Liu, C. Sun, M. Mann, A. S. Tang, M. C. Onbasli, D. Bono, P. M. Voyles, Y. Xu, J. Robinson, G. S. D. Beach, C. A. Ross, *Adv. Electron. Mater.* **2016**, *3*, 1600376.
[19] E. R. Rosenberg, L. Beran, C. O. Avci, C. Zeledon, B. Song, C. Gonzalez-Fuentes, J. Mendil, P. Gambardella, M. Veis, C. Garcia, G. S. D. Beach, C. A. Ross, *Phys. Rev. Mater.* **2018**, *2*, 094405.
[20] C. N. Wu, C. C. Tseng, Y. T. Fanchiang, C. K. Cheng, K. Y. Lin, S. L. Yeh, S. R. Yang, C. T. Wu, T. Liu, M. Wu, M. Hong, J. Kwo, *Sci. Rep.* **2018**, *8*, 11087.
[21] E. R. Rosenberg, K. Litzius, J. M. Shaw, G. A. Riley, G. S. D. Beach, H. T. Nembach, C. A. Ross, *Adv. Electron. Mater.* **2021**, *7*, 2100452.
[22] J. J. Bauer, E. R. Rosenberg, S. Kundu, K. A. Mkhoyan, P. Quarterman, A. J. Grutter, B. J. Kirby, J. A. Borchers, C. A. Ross, *Adv. Electron. Mater.* **2020**, *6*, 1900820.
[23] J. J. Bauer, E. R. Rosenberg, C. A. Ross, *Appl. Phys. Lett.* **2019**, *114*, 052403.
[24] C. O. Avci, E. Rosenberg, M. Baumgartner, L. Beran, A. Quindeau, P. Gambardella, C. A. Ross, G. S. D. Beach, *Appl. Phys. Lett.* **2017**, *111*, 072406.
[25] L. Caretta, S. H. Oh, T. Fakhrul, D. K. Lee, B. H. Lee, S. K. Kim, C. A. Ross, K. J. Lee, G. S. D. Beach, *Science* **2020**, *370*, 1438.

© 2023 Wiley-VCH GmbH

16136829, 0, Downloaded from https://onlinelibrary.wiley.com/doi/10.1002/smll.202300824 by Massachusetts Institute of Technolo, Wiley Online Library on [15/04/2023]. See the Terms and Conditions (https://onlinelibrary.wiley.com/terms-and-conditions) on Wiley Online Library for rules of use; OA articles are governed by the applicable Creative Commons License

[26] C. O. Avci, E. Rosenberg, L. Caretta, F. Büttner, M. Mann, C. Marcus, D. Bono, C. A. Ross, G. S. D. Beach, *Nat. Nanotechnol.* **2019**, *14*, 561.
[27] S. Ding, A. Ross, R. Lebrun, S. Becker, K. Lee, I. Boventer, S. Das, Y. Kurokawa, S. Gupta, J. Yang, G. Jakob, M. Kläui, *Phys. Rev. B* **2019**, *100*, 100406.
[28] T. Fakhrul, S. Tazlaru, B. Khurana, L. Beran, J. Bauer, M. Vančík, A. Marchese, E. Tsotsos, M. Kučera, Y. Zhang, M. Veis, C. A. Ross, *Adv. Opt. Mater.* **2021**, *9*, 2100512.
[29] H. J. van Hook, *J. Am. Ceram. Soc.* **1961**, *44*, 208.
[30] A. P. Galayda, N. E. Volkova, L. Y. Gavrilova, K. G. Balymov, V. A. Cherepanov, *J. Alloys Compd.* **2017**, *718*, 288.
[31] S. A. Manuilov, S. I. Khartsev, A. M. Grishin, *J. Appl. Phys.* **2009**, *106*, 123917.
[32] B. Khurana, J. J. Bauer, P. Zhang, T. Safi, C.-T. Chou, J. T. Hou, T. Fakhrul, Y. Fan, L. Liu, C. A. Ross, *Phys. Rev. Mater.* **2021**, *5*, 084408.
[33] L. Caretta, M. Mann, F. Büttner, K. Ueda, B. Pfau, C. M. Günther, P. Hessing, A. Churikova, C. Klose, M. Schneider, D. Engel, C. Marcus, D. Bono, K. Bagschik, S. Eisebitt, G. S. D. Beach, *Nat. Nanotechnol.* **2018**, *13*, 1154.
[34] J. Finley, L. Liu, *Phys. Rev. Appl.* **2016**, *6*, 054001.
[35] H.-A. Zhou, Y. Dong, T. Xu, K. Xu, L. Sánchez-Tejerina, L. Zhao, Y. Ba, P. Gargiani, M. Valvidares, Y. Zhao, M. Carpentieri, O. A. Tretiakov, X. Zhong, G. Finocchio, S. K. Kim, W. Jiang, *arXiv* **2019**, 1912.01775.
[36] L. Liensberger, A. Kamra, H. Maier-Flaig, S. Geprägs, A. Erb, S. T. B. Goennenwein, R. Gross, W. Belzig, H. Huebl, M. Weiler, *Phys. Rev. Lett.* **2019**, *123*, 117204.
[37] B. W. Dong, J. Cramer, K. Ganzhorn, H. Y. Yuan, E. J. Guo, S. T. B. Goennenwein, M. Klaui, *J. Phys. Condens. Matter* **2018**, *30*, 035802.
[38] (Eds: K.-H. Hellwege, A. M. Hellwege), *Landolt-Börnstein – Group III Crystal and Solid State Physics*, Vol. *12a*, Springer-Verlag, Berlin **1978**.
[39] Q. Shao, A. Grutter, Y. Liu, G. Yu, C.-Y. Yang, D. A. Gilbert, E. Arenholz, P. Shafer, X. Che, C. Tang, M. Aldosary, A. Navabi, Q. Lin He, B. J. Kirby, J. Shi, K. L. Wang, *Phys. Rev. B* **2019**, *99*, 104401.
[40] M. Kuila, Z. Hussain, V. R. Reddy, *J. Magn. Magn. Mater.* **2019**, *473*, 458.
[41] S. Damerio, C. O. Avci, arXiv preprint. **2023**, arXiv:2302.03758.
[42] Y. K. Liu, H. F. Wong, K. K. Lam, K. H. Chan, C. L. Mak, C. W. Leung, *J. Magn. Magn. Mater.* **2018**, *468*, 235.
[43] P. Hansen, *J. Appl. Phys.* **1974**, *45*, 3638.
[44] M. Oron, I. Barlow, W. F. Traber, *J. Mater. Sci.* **1969**, *4*, 271.
[45] A. Albinati, B. T. M. Willis, *J. Appl. Crystallogr.* **1982**, *15*, 361.
[46] C. B. Arnold, M. J. Aziz, *Appl. Phys. A* **1999**, *69*, S23.
[47] T. Bayaraa, C. Xu, D. Campbell, L. Bellaiche, *Phys. Rev. B* **2019**, *100*, 214412.
[48] R. D. Cowan, *Theory of Atomic Structure and Spectra*, University Of California Press, California **1981**.
[49] G. Van Der Laan, *J. Electron Spectrosc. Relat. Phenom.* **1997**, *86*, 41.
[50] P. H. Butler, *Point Group Symmetry Applications: Methods and Tables*, Plenum Press, New York **1981**.
[51] E. Stavitski, D. Groot, *Micron* **2010**, *41*, 687.
[52] C. Carvallo, P. Sainctavit, M. A. Arrio, N. Menguy, Y. Wang, G. Ona-Nguema, S. Brice-Profeta, *Am. Mineral.* **2008**, *93*, 880.
[53] G. Cressey, C. M. B. Henderson, G. van der Laan, *Phys. Chem. Miner.* **1993**, *20*, 111.
[54] P. Kuiper, B. G. Searle, L. C. Duda, R. M. Wolf, P. J. Van Der Zaag, *J. Electron Spectrosc. Relat. Phenom.* **1997**, *86*, 107.
[55] B. Ravel, M. Newville, *J. Synchrotron Radiat.* **2005**, *12*, 537.
[56] (Eds: J. C. Fuggle, J. E. Inglesfield), *Unoccupied Electronic States*, Springer Berlin Heidelberg, Berlin **1992**.
[57] F. M. F. De Groot, J. C. Fuggle, B. T. Thole, G. A. Sawatzky, *Phys. Rev. B* **1990**, *42*, 5459.
[58] H. B. Vasili, B. Casals, R. Cichelero, F. Macià, J. Geshev, P. Gargiani, M. Valvidares, J. Herrero-Martin, E. Pellegrin, J. Fontcuberta, G. Herranz, *Phys. Rev. B* **2017**, *96*, 014433.
[59] Z. Zheng-Wu, W. Ping-Feng, Y. Jian-Hua, Z. Kang-Wei, *Phys. Rev. B* **1993**, *48*, 16407.
[60] B. Liu, C. Piamonteze, M. U. Delgado-Jaime, R. P. Wang, J. Heidler, J. Dreiser, R. Chopdekar, F. Nolting, F. M. F. De Groot, *Phys. Rev. B* **2017**, *96*, 054446.
[61] F. M. F. de Groot, A. Kotani, *Core Level Spectroscopy of Solids*, CRC Press, Boca Raton, FL **2008**.
[62] T. Su, S. Ning, E. Cho, C. A. Ross, *Phys. Rev. Mater.* **2021**, *5*, 094403.
[63] B. T. Thole, G. van der Laan, J. C. Fuggle, G. A. Sawatzky, R. C. Karnatak, J.-M. Esteva, *Phys. Rev. B* **1985**, *32*, 5107.
[64] R. Biagi, J. Fernandez-Rodriguez, M. Gonidec, A. Mirone, V. Corradini, F. Moro, V. De Renzi, U. Del Pennino, J. C. Cezar, D. B. Amabilino, J. Veciana, *Phys. Rev. B: Condens. Matter Mater. Phys.* **2010**, *82*, 224406.
[65] T. Fakhrul, S. Tazlaru, B. Khurana, L. Beran, J. Bauer, M. Vančík, A. Marchese, E. Tsotsos, M. Kučera, Y. Zhang, M. Veis, C. A. Ross, T. Fakhrul, B. Khurana, J. Bauer, A. Marchese, E. Tsotsos, Y. Zhang, C. A. Ross, S. Tazlaru, L. Beran, M. Vančík, M. Kučera, M. Veis, *Adv. Opt. Mater.* **2021**, *9*, 2100512.
[66] M. Balaguer, C.-Y. Yoo, H. J. M. Bouwmeester, J. M. Serra, *J. Mater. Chem. A* **2013**, *1*, 10234.
[67] J. E. R. Ibarra, *Magnetic Ions-Doped Zno Nanocrystals: Study of the Structural, Electronic, Optical and Magnetic Properties*, Universidade de Brasilia, Brazil **2018**.
[68] B. M. Reddy, P. Saikia, P. Bharali, Y. Yamada, T. Kobayashi, M. Muhler, W. Grü, *J. Phys. Chem. C* **2008**, *112*, 16393.
[69] H. Ogasawara, A. Kotani, B. T. Thole, *Phys. Rev. B* **1994**, *50*, 12332.
[70] W. Zhonghua, L. Kunquan, D. Jun, L. Fenyu, F. Zhengmin, F. Zhengzhi, *Zeitschrift für Phys. B Condens. Matter* **1991**, *82*, 15.
[71] X. Biquard, E. G. Víllora, K. Shimamura, K. Lorenz, *J. Appl. Phys.* **2020**, *127*, 115106.
[72] G. F. Dionne, *J. Appl. Phys.* **1970**, *41*, 4874.
[73] G. F. Dionne, *Magnetic Moment Versus Temperature Curves of Rare-Earth Iron Garnets*, Springer, Lexington, MA **1979**.
[74] S. J. Tan, W. Zhang, L. Yang, J. Chen, Z. Wang, *J. Appl. Phys.* **2020**, *128*, 183904.
[75] J. Salmon, Z. Harmany, C. A. Deledalle, R. Willett, *J. Math. Imaging Vis.* **2014**, *48*, 279.

16136829, 0, Downloaded from https://onlinelibrary.wiley.com/doi/10.1002/smll.202300824 by Massachusetts Institute of Technolo, Wiley Online Library on [15/04/2023]. See the Terms and Conditions (https://onlinelibrary.wiley.com/terms-and-conditions) on Wiley Online Library for rules of use; OA articles are governed by the applicable Creative Commons License